Medical Physics
The International Journal of Medical Physics Research and Practice

Development of a registration framework to validate MRI with histology for prostate focal therapy

H. M. Reynolds, S. Williams, A. Zhang, R. Chakravorty, D. Rawlinson, C. S. Ong, M. Esteva, C. Mitchell, B. Parameswaran, M. Finnegan, G. Liney, and A. Haworth

Citation: Medical Physics **42**, 7078 (2015); doi: 10.1118/1.4935343
View online: http://dx.doi.org/10.1118/1.4935343
View Table of Contents: http://scitation.aip.org/content/aapm/journal/medphys/42/12?ver=pdfcov
Published by the American Association of Physicists in Medicine

Development of a registration framework to validate MRI with histology for prostate focal therapy

H. M. Reynolds[a)]
Department of Physical Sciences, Peter MacCallum Cancer Centre, East Melbourne, Victoria 3002, Australia and Sir Peter MacCallum Department of Oncology, University of Melbourne, East Melbourne, Victoria 3002, Australia

S. Williams
Department of Pathology, University of Melbourne, Parkville, Victoria 3010, Australia and Division of Radiation Oncology and Cancer Imaging, Peter MacCallum Cancer Centre, East Melbourne, Victoria 3002, Australia

A. Zhang, R. Chakravorty, and D. Rawlinson
Electrical and Electronic Engineering, University of Melbourne, Parkville, Victoria 3010, Australia

C. S. Ong
Electrical and Electronic Engineering, University of Melbourne, Parkville, Victoria 3010, Australia; Machine Learning Research Group, National ICT Australia, Canberra 2601, Australia; and Research School of Computer Science, Australian National University, Canberra 2601, Australia

M. Esteva
Electrical and Electronic Engineering, University of Melbourne, Parkville, Victoria 3010, Australia

C. Mitchell
Department of Pathology, Peter MacCallum Cancer Centre, East Melbourne, Victoria 3002, Australia

B. Parameswaran
Division of Radiation Oncology and Cancer Imaging, Peter MacCallum Cancer Centre, East Melbourne, Victoria 3002, Australia

M. Finnegan
Department of Physical Sciences, Peter MacCallum Cancer Centre, East Melbourne, Victoria 3002, Australia

G. Liney
Ingham Institute for Applied Medical Research, Liverpool Hospital, New South Wales 2170, Australia

A. Haworth
Department of Physical Sciences, Peter MacCallum Cancer Centre, East Melbourne, Victoria 3002, Australia and Sir Peter MacCallum Department of Oncology, University of Melbourne, East Melbourne, Victoria 3002, Australia

(Received 16 April 2015; revised 17 September 2015; accepted for publication 25 October 2015; published 19 November 2015)

Purpose: Focal therapy has been proposed as an alternative method to whole-gland treatment for prostate cancer when aiming to reduce treatment side effects. The authors recently validated a radiobiological model which takes into account tumor location and tumor characteristics including tumor cell density, Gleason score, and hypoxia in order to plan optimal dose distributions for focal therapy. The authors propose that this model can be informed using multiparametric MRI (mpMRI) and in this study present a registration framework developed to map prostate mpMRI and histology data, where histology will provide the "ground truth" data regarding tumor location and biology. The authors aim to apply this framework to a growing database to develop a prostate biological atlas which will enable MRI based planning for prostate focal therapy treatment.

Methods: Six patients scheduled for routine radical prostatectomy were used in this proof-of-concept study. Each patient underwent mpMRI scanning prior to surgery, after which the excised prostate specimen was formalin fixed and mounted in agarose gel in a custom designed sectioning box. T2-weighted MRI of the specimen in the sectioning box was acquired, after which 5 mm sections of the prostate were cut and histology sections were microtomed. A number of image processing and registration steps were used to register histology images with *ex vivo* MRI and deformable image registration (DIR) was applied to 3D T2w images to align the *in vivo* and *ex vivo* MRI data. Dice coefficient metrics and corresponding feature points from two independent annotators were selected in order to assess the DIR accuracy.

Results: Images from all six patients were registered, providing histology and *in vivo* MRI in the *ex vivo* MRI frame of reference for each patient. Results demonstrated that their DIR methodology to register *in vivo* and *ex vivo* 3D T2w MRI improved accuracy in comparison with an initial manual

alignment for prostates containing features which were readily visible on MRI. The average estimated uncertainty between *in vivo* MRI and histology was 3.3 mm, which included an average error of 3.1 mm between *in vivo* and *ex vivo* MRI after applying DIR. The mean dice coefficient for the prostate contour between *in vivo* and *ex vivo* MRI increased from 0.83 before DIR to 0.93 after DIR. **Conclusions:** The authors have developed a registration framework for mapping *in vivo* MRI data of the prostate with histology by implementing a number of processing steps and *ex vivo* MRI of the prostate specimen. Validation of DIR was challenging, particularly in prostates with few or mostly linear rather than spherical shaped features. Refinement of their MR imaging protocols to improve the data quality is currently underway which may improve registration accuracy. Additional mpMRI sequences will be registered within this framework to quantify prostate tumor location and biology.
 [http://dx.doi.org/10.1118/1.4935343]

Key words: deformable image registration, multiparametric MRI, histology, focal therapy, prostate cancer

1. INTRODUCTION

Focal therapy has been proposed as an alternative method to whole-gland treatment for prostate cancer.[1] Brachytherapy, using permanently implanted radioactive I-125 seeds, provides a method for treating prostate subvolumes with high doses of radiation whilst sparing healthy surrounding tissue. Various methods for defining these subvolumes have been proposed[2] and the results of a pilot study using a subvolume defined by biopsy and MRI with a "large safety margin" have recently been reported.[3]

To minimize the amount of healthy tissue receiving a high radiation dose requires accurate tumor delineation. In addition, due to the multifocal nature of prostate cancer, even small tumors that demonstrate a high Gleason score may need to be incorporated into high dose regions to minimize the risk of local recurrence.[4] We have recently proposed and validated a radiobiological model which can be used to predict the radiation dose that is required to adequately treat prostate cancers.[5] This model requires knowledge of tumor location and tumor specific characteristics including tumor cell density (TCD), tumor proliferation which can be related to Gleason score (GS), and hypoxia (H). In order to apply this model clinically, *in vivo* multiparametric MRI (mpMRI) is required to give voxel level information about each of these parameters.

Various investigators have demonstrated the ability of mpMRI to predict tumor location, TCD, GS, and H through correlation with "ground truth" histology data.[6–12] Histological validation is important for interpretation and characterization of prostate tissue shown on MRI, as histological samples provide a direct visualization of cellular characteristics and tissue structure and can be scanned in color on a micrometer scale. In contrast, MR images are typically at millimeter resolution and the signal is an indirect representation of tissue structure determined by proton density and energy exchange between hydrogen nuclei, which is also influenced by sequence and machine specific parameters. Accurate registration of MRI with histology is therefore important and has benefits for various research and clinical applications including the following: improved targeting for image guided prostate biopsy; accurate cancer diagnosis, grading, and tumor localization; and for clinical trials to assess the performance of novel imaging methods.

Despite these benefits, many correlation studies of the prostate have been limited in their predictive power, due to uncertainties and simplistic assumptions in the registration of histology with mpMRI,[6,9–13] and restriction to assessing the peripheral zone rather than the entire prostate gland.[7,8] In a review paper by Meyer *et al.*,[14] a number of approaches to registration of *in vivo* MRI and histology with assumptions that limit coregistration accuracy were described. These approaches included (1) simplistic visual correspondence of histology images with MRI slices and (2) registration of histology with manually or automatically selected corresponding *in vivo* MRI slices. While the second approach can adjust for in-plane deformation, neither approach is able to account for out-of-plane deformation caused by surgery or histological processing, and incorrectly assumes registration of prostate *in vivo* MRI with histology is less than a fully nonlinear 3D problem.

Studies that assume a direct slice correspondence between histology and *in vivo* MRI include that by Chappelow *et al.*[15] who developed an elastic registration technique using a multivariate formulation utilizing all mpMRI data to match with histology while Nir *et al.*[16] implemented a particle filtering framework to determine the optimal location of an imaging volume slice to match each histology image. In work by Turkbey *et al.*,[17] custom molds were made for the prostate specimen using *in vivo* MR images, to guide pathological sectioning. *In vivo* MRI slices were then matched visually with histology, and misalignment was adjusted for by assessing neighboring regions.

To guide the registration of *in vivo* MRI with histology and adjust for out-of-plane deformation, imaging of the prostate specimen using *ex vivo* MRI or block face photos of the specimen is preferable.[14] Such approaches have often used fiducial markers in the specimen to facilitate reconstruction of histology or block face photos into 3D.[18,19] In a study by Ward *et al.*,[20] strand-shaped fiducial markers were placed on the prostate specimen and *ex vivo* 3D T2w MRI obtained, to determine the optimal cutting plane to match specimen sectioning with *in vivo* MRI slices. In work by Groenendaal *et al.*,[7] three carbon rods were inserted into the prostate specimen and used to assist registration. Rigid and deformable registration

methods were used to map the reconstructed specimen with *in vivo* MRI. Errors of 2–3 mm between MRI and histology were reported; however, a 5 mm margin was still required for MR tumor delineations to accurately correlate with tumors shown in histology. Recently, biomechanical modeling methods for registration purposes have been investigated. Studies by Nir *et al.*[21] and Samavati *et al.*[22] used magnetic resonance elastography data to derive material properties for deformable registration of *in vivo* MRI with *ex vivo* MRI. Average errors between *in vivo* MRI and histology between 2 and 3 mm were obtained and although results were promising, further investigation is required due to limited sample size.

In order to remove the need to rely on direct slice to slice correspondences, Park *et al.* developed a method to register MRI with histology using both block face photos and *ex vivo* MRI of the prostate specimen. Their method implemented multiple registration tasks, to take into account each aspect of tissue deformation including fixation and histology processing, without the use of fiducial markers in the prostate specimen. Deformable registration was implemented using mutual information and thin plate splines to register stacked block face photos with *ex vivo* MRI, and then subsequently to map *ex vivo* MRI with *in vivo* MRI. Errors between points in diffusion MRI and histology of 3.74 and 2.26 mm were reported for two proof-of-concept patients.[23] In a later study, Park *et al.* presented results for mapping between MRI and ^{11}C-choline PET, again using *ex vivo* MRI.[24] Despite taking many aspects of deformation into account, this approach suffered from uncertainties regarding the slice thickness of the specimen sections relative to *ex vivo* MRI and utilized custom-made software that was not freely available and difficult to run on modern platforms.

In our work, we aimed to implement and build upon the approach of Park *et al.*, by similarly taking into account each aspect of prostate deformation via a series of registration tasks. We have treated the deformation between *in vivo* and *ex vivo* MRI as a 3D problem, without utilizing fiducials in the specimen to reduce interference with the prostate. In contrast to Park *et al.*, however, we have not utilized block face photos but instead designed a custom sectioning box which we used on all specimens during *ex vivo* MRI scanning and to provide control over parallel tissue sectioning thickness. We have used open source and commonly used software to develop the framework, acquiring *in vivo* and *ex vivo* 3D T2w images and applying deformable registration to align them after implementing a novel step by convolving images with a Laplacian of Gaussian (LoG) filter to reduce noise and extract features to guide the registration. This registration step aimed to correct for tissue shrinkage and deformation after surgical removal. *Ex vivo* MR scanning included an axial T2w image at high in-plane resolution with slices we assumed matched histology sections. Each 2D histology image was registered with its corresponding *ex vivo* axial T2w image to account for formalin fixation and histology processing, initially aligned by using a similarity transform guided by matching control points, followed by an automatic registration. The following describes our developed framework in detail and provides metrics validating the approach.

2. METHODS

For this proof-of-concept study, we report on a sample set of six patients with biopsy proven prostate cancer scheduled for radical prostatectomy. Study approval was obtained from our institutional review board and informed consent was obtained from all patients.

2.A. Patient data

As detailed in Table I, patient age ranged from 55 to 71 years, pathological Gleason score 6–9, PSA 6.0–17.3 ng/ml, pathological T stage 2c to 3b. Presurgical mpMRI was carried out on all patients at least 4 weeks (range 30–93 days) postbiopsy and no more than 44 days (average 20 days) prior to surgical removal of the prostate. Surgical specimens were embedded in agarose gel and *ex vivo* MRI acquired within 24 h after prostatectomy. Whole mount histology sections were then obtained from the prostate specimen.

2.B. *In vivo* MR imaging

In vivo mpMRI data were collected for all patients based on the European Society of Urogenital Radiology (ESUR) guidelines[25] using a 3T Siemens Trio Tim machine (Siemens Medical Solutions, Erlangen, Germany). The protocol included T2w, diffusion weighted imaging (DWI), and dynamic contrast-enhanced MRI (DCE-MRI), taking between 35 and 40 min of scanning time. A torso surface coil was used during data acquisition, without the use of an endorectal coil to minimize deformation of the prostate. An axial T2w image was acquired as per normal clinical protocol with an in-plane resolution of 0.5×0.5 mm as shown in Fig. 1(a) (turbo spin-echo, $TR/TE = 3500/96$ ms, echo train length = 23, acquisition matrix = 320×320, FOV = 160×160 mm, slice thickness = 3 mm, intersection gap = 0.75 mm). In addition, a 3D T2w image was acquired at a resolution of $0.62\times0.62\times0.6$ mm [turbo spin-echo, $TR/TE = 750/(104–110)$ ms, echo train length = 21, acquisition matrix = 384×384, FOV = 240×240 mm] for the purpose of registration with *ex vivo* 3D T2w MRI.

2.C. Specimen preparation

After prostatectomy, specimens were formalin fixed, weighed, and surfaced inked as per routine clinical protocol.

TABLE I. Details of each study patient.

Patient	Age	Gleason score (and grades)	PSA	Pathological T stage	Prostate weight (g)	Total tumor volume (mm^3)
1	58	7 (3+4)	6.49	pT3a	48	4 900
2	62	9 (5+4) and 6 (3+3)	9.4	pT3b	60	19 700
3	55	7 (3+4)	7.2	pT3a	47	3 000
4	71	6 (3+3)	8.8	pT2c	76	<1 000
5	59	7 (3+4)	6.0	pT2c	42	7 480
6	67	7 (4+3, tertiary 5)	17.3	pT3b	63	30 100

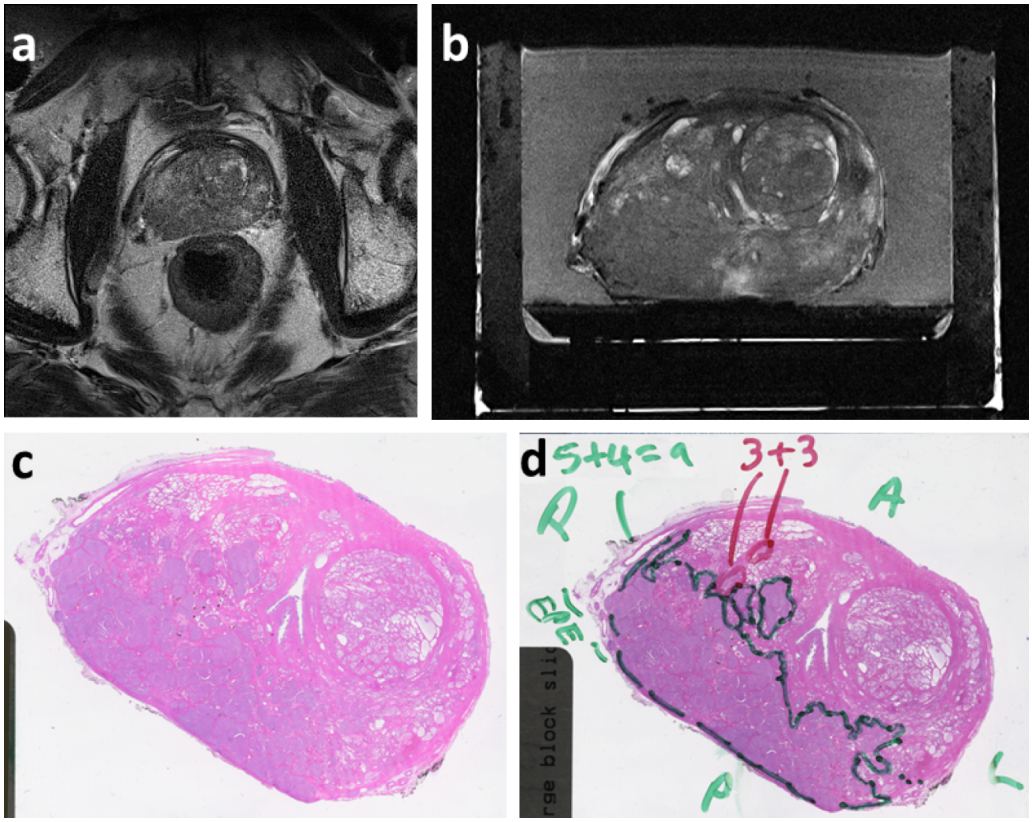

FIG. 1. Example of the MRI and histology data (a) *in vivo* axial T2w MRI, (b) *ex vivo* axial T2w MRI, and (c) unannotated and (d) annotated H&E stained histology images.

The specimen was placed into a custom-made sectioning box which contained slots every 5 mm to guide the pathologist's knife after *ex vivo* MR imaging (Fig. 2). The prostate was positioned so that sections would be cut axially from the apex to the base and was fixed in place by embedding in agarose gel.

2.D. *Ex vivo* MR imaging

Two sets of *ex vivo* T2w images at different resolutions were acquired for each patient, (1) a 3D T2w dataset to register with *in vivo* 3D T2w data and (2) a high resolution, axial T2w dataset to register with histology images. Data acquisition of the prostate specimen in the sectioning box was carried out using an 8-channel knee coil and took approximately 25 min including setup time. First, T1 coronal images were obtained at resolution $0.42 \times 0.42 \times 0.03$–$0.15$ mm [turbo spin echo, $TR/TE = (972$–$1450)/10$ ms, echo train length = 4, acquisition matrix = 384×270, FoV 112.5×160 mm] to provide detail of the sectioning box slot locations. Axial T2w images were then acquired by using the T1 coronal images to orient the slice geometry to ensure every second axial image aligned with the cutting planes in the sectioning box, and thereby matched the sections cut in pathology [Fig. 2(b)]. The axial T2w images had an in-plane resolution of 0.22 mm and slice thickness 2.5 mm (turbo spin-echo, $TR/TE = 3670/76$ ms,

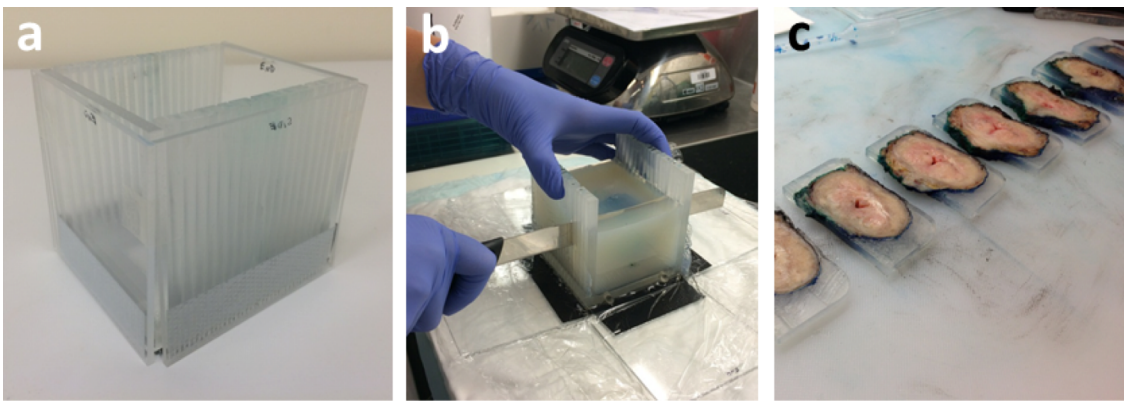

FIG. 2. (a) Custom-made box for *ex vivo* MRI scanning and specimen sectioning, (b) embedded prostate sectioning, and (c) the resultant prostate slices.

echo train length = 20, acquisition matrix = 448 × 312, FOV = 100 × 69.6 mm). For patients 4–6, the process of matching MRI slices to histology was aided by placing a MRI-visible fiducial marker between the location of the first and second cuts made in pathology. The *ex vivo* 3D T2w image dataset was then acquired at the same resolution as the *in vivo* 3D T2w images to use in coregistration; however, the option to interpolate the data in-plane before image reconstruction was selected in the scan protocol, resulting in an interpolated sampling interval with an apparent resolution of 0.31 × 0.31 × 0.6 mm [turbo spin-echo, $TR/TE = 750/(110–117)$ ms, echo train length = 21, FOV = 172.5 × 200 mm, acquisition matrix = 268 × 320 mm with the "interpolate" function on].

2.E. Histopathology data

After *ex vivo* MR imaging, the prostate specimen was cut into 5 mm blocks using the knife-guiding slots in the sectioning box. Each 5 mm thick block was embedded in paraffin, and a 3 μm thick section was microtomed from the top surface of each block. Typically, a few sections of 20 μm required cutting from this top surface before a full face of tissue at 3 μm thickness could be obtained. Once a 3 μm thick section per block was acquired it was whole mounted on a 25 × 75 mm slide and stained with haematoxylin and eosin (H&E). Unmarked H&E slides were scanned on an Epson Perfection V700 scanner (Epson, Suwa, Japan) to give images at approximately 0.01 mm resolution [Fig. 1(c)].

An expert pathologist (CM) annotated tumor foci on each H&E slide, including the Gleason score, with a dark pen [Fig. 1(d)]. These annotated slides were also scanned on the Epson Perfection V700 scanner to provide a digitized image of the tumor location. Tumor annotations were wiped off using alcohol, and peripheral zone outline annotations were drawn by the same pathologist with dark pen on the slides and scanned to give digitized histology images of the peripheral zone location.

2.F. Image registration overview

To combine image datasets from each patient into a single frame of reference, a series of image processing and registration tasks were carried out. A schematic showing how each image set was related is shown in Fig. 3, where the *ex vivo* axial T2w MRI dataset was taken as the referent image.

2.G. *In vivo* MRI registration

The amount of movement between the *in vivo* axial and 3D MRI scans was minimal, as images were acquired during the same scanning session for each patient. Therefore, a rigid registration using the BRAINS registration module[26] with mutual information as the similarity metric in 3D SLICER software (http://www.slicer.org)[27] was used due to the ease of implementation, to align the *in vivo* T2w MRI datasets. In cases where visual assessment of the registration was inadequate due to bladder filling or rectal motion, a manual rigid registration of the images was implemented.

2.H. *In vivo* to *ex vivo* MRI registration

To aid the challenging task of registering *in vivo* MRI to *ex vivo* MRI, images were preprocessed using a 3D LoG filter. The following steps describe the methods applied:

1. The prostate capsule was manually contoured on the axial T2w *in vivo* and *ex vivo* MR images by a radiation oncologist experienced in prostate contouring (SW) to provide a prostate mask. Each mask was then interpolated and resampled to match the resolution of the 3D

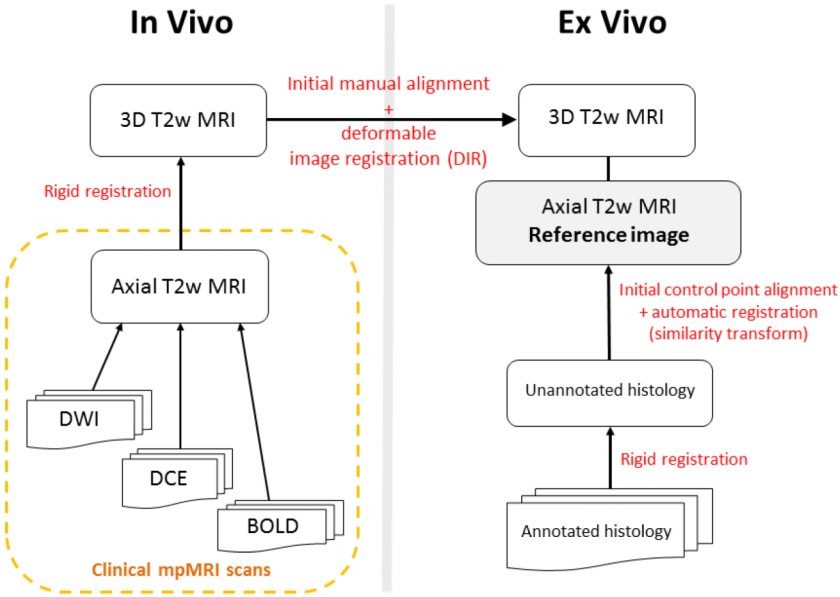

FIG. 3. Schematic demonstrating how MRI data and histology images are registered. The axial *ex vivo* T2w image for each patient forms the reference data set with which all other images are coregistered.

T2w datasets. Rigid registration was applied to align the prostate contour mask with the 3D T2w MRI before it was resampled; however, there was no movement of the specimen between the *ex vivo* axial and 3D scans, therefore registration was not required before the *ex vivo* mask image was resampled.

2. To ensure the registration was driven by dominant features within the prostate which were more likely visible on both *in vivo* and *ex vivo* MRI, both the *in vivo* and *ex vivo* 3D T2w MR images were convolved with a 3D LoG kernel using ImageJ.[28,29] This kernel also had the effect of reducing noise in the image data. The 3D LoG images were then cropped at the prostate contour boundary using the 3D mask images from step 1 (as shown in Fig. 4).
3. An initial manual alignment of the prostate between the *in vivo* 3D MRI and *ex vivo* 3D MRI data was applied using a 9 degree of freedom (DOF) transformation, which included rotation, translation, and scaling in some cases where shrinkage was seen, similar to that observed in a study by Orczyk *et al.*[30] who compared *in vivo* and *ex vivo* prostate volumes and shapes. A manual approach was preferred over an automatic method to provide more control over the alignment before deformable image registration (DIR) was applied. The *in vivo* 3D LoG filtered image was aligned with the *ex vivo* 3D MRI using the same 9 DOF transformation.
4. DIR was performed in 3D using an algorithm introduced by Rueckart *et al.*[31,32] in CMTK software (http://www.nitrc.org/projects/cmtk) with the *in vivo* 3D LoG filtered and masked image as the moving image and the *ex vivo* 3D LoG filtered and masked image as the reference image. This involved a transformation model based on cubic spline interpolation between sparse, uniformly distributed control points and implemented a normalized mutual information similarity metric over the entire imaging volume. Parameters were chosen empirically and were the same across all patients, including a rigidity constraint to reduce unrealistic deformations.
5. Finally, the DIR transformation computed in step 4 was applied to the manually aligned *in vivo* 3D T2w MRI to deformably register it to *ex vivo* 3D T2w MRI.

2.I. Histology to *ex vivo* MRI registration

All histology to *ex vivo* MRI registration was carried out using MATLAB software (MATLAB 8.4, The MathWorks, Inc., Natlick, MA). First, annotated histology images with tumor markings and histology images including the peripheral zone markings were registered with the unannotated histology image using an intensity based rigid registration, with mutual information as the similarity metric. Since these images were obtained from the same histology slide, no deformation was required. Binary tumor and peripheral zone mask images were created from the annotated histology images in GIMP software (GNU Image Manipulation Program) by manually tracing around the annotation lines and converting to masks. These mask images were registered with unannotated histology using the rigid transformation computed for the corresponding annotated histology image.

To register histology data with *ex vivo* MRI, we assumed each histology section matched an *ex vivo* axial T2w image due to the sectioning box design which provided matching of the slice orientation during scanning using the T1 coronal images. We also assumed that deformations of the histology sample during processing could be described by a nonreflective similarity transformation with rotation, translation, and uniform scaling. This method expected that any stretching of the tissue was uniform and was deemed appropriate

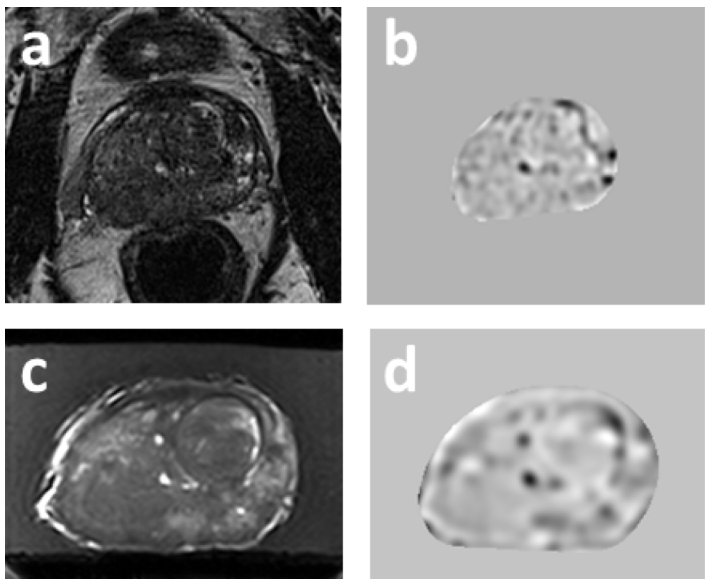

FIG. 4. Example slices from the (a) *in vivo* 3D T2w MRI and (c) *ex vivo* 3D T2w MRI with its corresponding (b) *in vivo* LoG filtered and masked image, and (d) *ex vivo* LoG filtered and masked image.

based on research by Gibson *et al.*[33] who quantified errors in tissue deformation between histology and *ex vivo* MRI data.

To initialize the registration between histology and *ex vivo* MRI, control points were chosen by selecting features that were easily identifiable on both image sets. Features included the centre of cystic structures which were bright on T2w images and white on histology, the centre of the urethra and the ejaculatory ducts, and the boundaries of the prostate (see Fig. 5). A similarity transformation was then computed for each histology section, by minimizing the Euclidean distance between the selected control points. Automatic registration using mutual information and a similarity transformation was then applied to complete the alignment. Additional preprocessing was required to guide this automated registration step by applying a background threshold to mask the histology image, which was also applied to the *ex vivo* MR image to mask out the sectioning box and agar gel.

2.J. Registration validation

To quantify the registration performance between *in vivo* and *ex vivo* 3D T2w MRI, we computed the Dice coefficient of the prostate boundary contour between the initial manually aligned and deformably registered images. However, given that the manual prostate boundary contours contributed to the computed registration, we also sought to validate the approach by additional measures. For this, we computed errors between a set of corresponding ground-truth feature points annotated on the unregistered *in vivo* 3D T2w MR and *ex vivo* 3D T2w MR images by two independent observers, a radiation oncologist (SW) and a radiologist (BP). Mean distance between point feature correspondences were computed both after initial manual alignment and after DIR.

We also assessed the registration accuracy of the peripheral zone, as while this is the most common location for tumors in the prostate, it tended to contain few feature points which could drive the registration. In order to do this, we assessed the location of the peripheral zone on *in vivo* axial T2w MRI which were annotated by a radiologist (BP) and the peripheral zone boundaries annotated on each histology slide by a pathologist (CM). These annotations were registered with the referent *ex vivo* axial T2w image and compared.

The more simple registration processes between histology images and *ex vivo* MRI were assessed quantitatively by computing the distance between control points after registration and visually by considering tissue structures and the prostate boundary. This included the accuracy of the alignment of unannotated histology images with the following: (1) the annotated histology images (both the tumor location and peripheral zone images) and (2) the *ex vivo* MRI.

3. RESULTS

Registration was carried out on all six patients, despite differences in prostate volume and severity of disease. Figure 6 shows the registration results for patient 2, demonstrating the deformed *in vivo* 3D T2w MRI data registered with histology

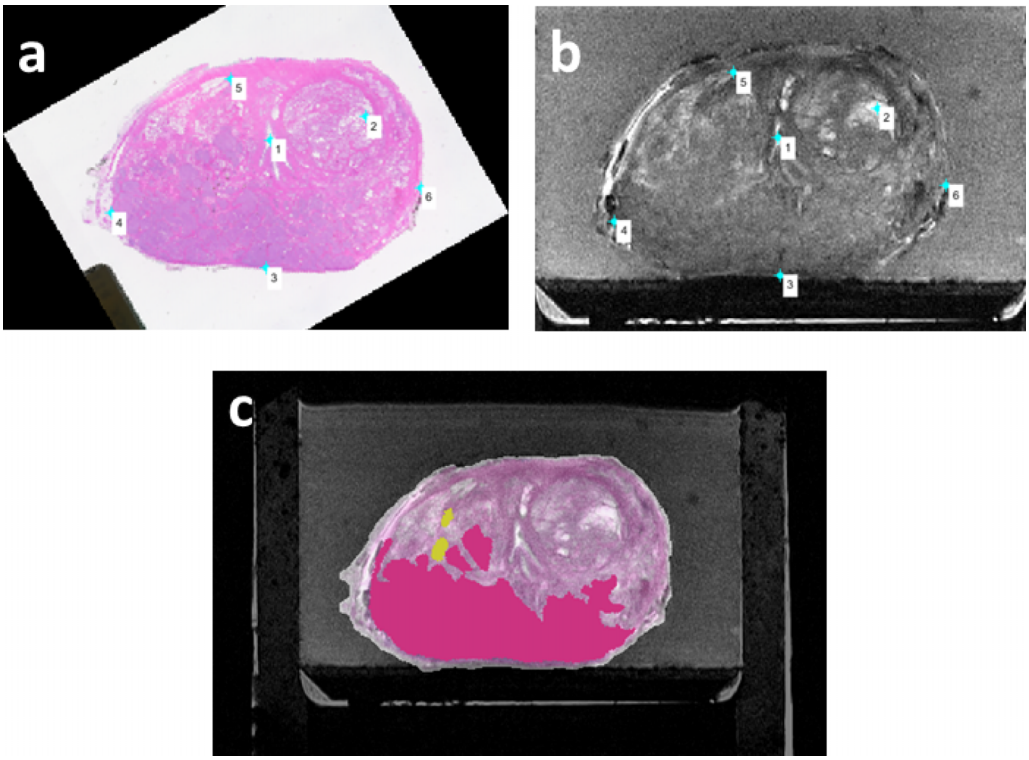

FIG. 5. Manually selected control points used to provide an initial registration between corresponding (a) unannotated histology image and (b) *ex vivo* MRI; (c) the final registered *ex vivo* MRI and histology image with the tumor annotation mask overlaid.

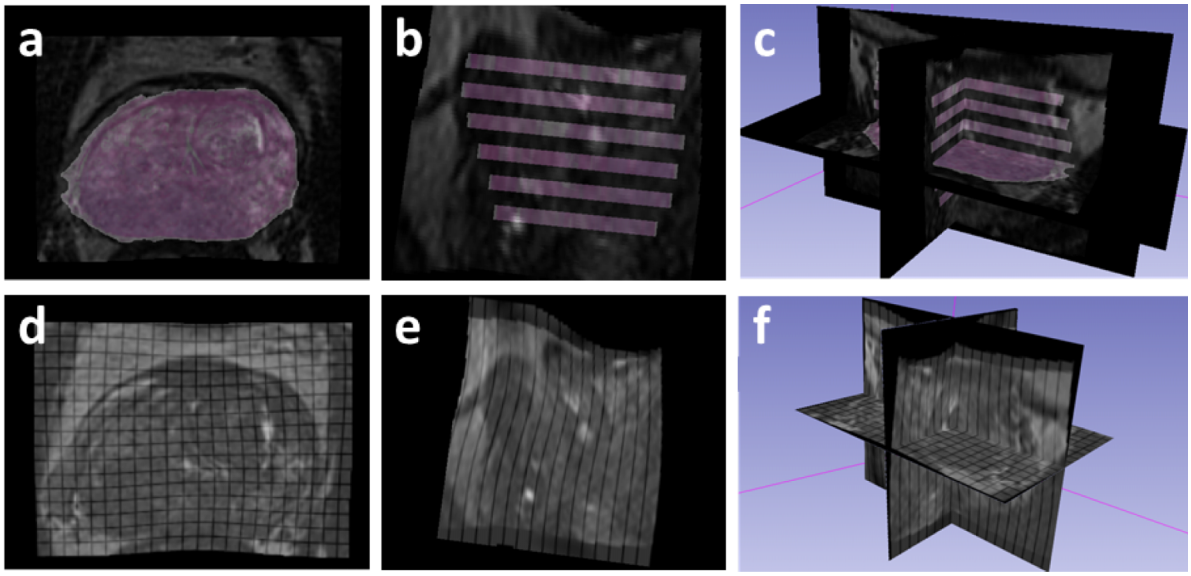

FIG. 6. Registration for patient 2 showing [(a)–(c)] axial, sagittal, and perspective views of *in vivo* 3D T2w MRI registered with histology, which is visualized with an interpolated slice thickness of 2.5 mm. [(d)–(f)] Axial, sagittal, and perspective views showing the nonlinear DIR grid map computed to register the *in vivo* and *ex vivo* MRI datasets, displayed on the *in vivo* 3D T2w MRI volume.

and the nonlinear DIR map overlaid on the *in vivo* 3D T2w MRI.

3.A. *In vivo* to *ex vivo* MRI registration

Table II presents the dice coefficient values between the *in vivo* and *ex vivo* prostate contours before and after DIR. On average, the dice coefficient was 0.83 when images were manually aligned with scaling applied (0%–18%), while after DIR, the average dice coefficient increased to 0.93. Furthermore, each individual patient had an improved dice coefficient after DIR in comparison with the initial manual alignment, with a minimum of 0.91 and maximum of 0.94.

Average errors computed between corresponding feature points selected by the two separate annotators are given in Table III. Annotator 1 chose as many points as they could see, with an average of ten points per patient, distributed throughout the prostate and frequently at the edge of visible nodules and internal prostate boundaries. Annotator 2 aimed to choose five points per patient (except for patient 3 where they could only confidently select two points) that could be reliably identified in both data sets at the centre of hyperintense regions on the T2w images and were mostly in the transition zone where adenomatous structures were frequently present.

TABLE II. Dice coefficients of the prostate contours between *in vivo* and *ex vivo* 3D T2w MRI and the peripheral zone contours (with standard deviation in brackets) between histology and *in vivo* MRI, before and after DIR.

	Prostate contours		Peripheral zone	
Patient	Before DIR	After DIR	Before DIR	After DIR
1	0.85	0.94	0.70 (0.09)	0.80 (0.04)
2	0.80	0.91	0.73 (0.10)	0.73 (0.18)
3	0.82	0.93	0.77 (0.12)	0.76 (0.08)
4	0.88	0.93	0.52 (0.24)	0.62 (0.28)
5	0.80	0.93	0.77 (0.06)	0.81 (0.05)
6	0.84	0.94	0.68 (0.15)	0.81 (0.06)
Average	**0.83**	**0.93**	**0.69 (0.13)**	**0.75 (0.12)**

Average feature point error based on those chosen by annotator 1 was 3.2 mm (SD 1.3 mm) after initial manual alignment and 3.2 mm (SD 1.6 mm) after DIR, while the average error from points chosen by annotator 2 was 4.1 mm (SD 1.4 mm) after initial manual alignment and 3.0 mm (SD 1.1 mm) after DIR. Overall, feature points selected by both annotators for patients 1, 4, 5, and 6 showed an improvement in image alignment after DIR with an average error of 3.8 mm (range 2.2–5.7 mm) for the initial manual alignment and 2.9 mm (range 2.0–5.1 mm) after DIR had been applied, while the average feature point error from both annotators between feature points for patient 3 was better before DIR. Patient 2, who had a large and aggressive tumor (see Table I) had conflicting results. Feature points selected by annotator 1 demonstrated the error increased from an average 2.4 to 3.2 mm after DIR, while feature points from annotator 2 showed a large decrease in error from 5.1 to 1.4 mm.

Dice coefficient values between peripheral zone contours before and after DIR are given in Table II. The average peripheral zone dice coefficient was 0.69 (SD 0.13) after the initial manual alignment and 0.75 (SD 0.12) after DIR, giving an average improvement of 6%. Most patients demonstrated an increase in peripheral zone overlap, except for patient 2 whose dice coefficient value remained the same and patient 3 whose dice coefficient reduced from 0.77 to 0.76 after DIR. This particular patient had a small prostate with only three histology slides available to compute overlap statistics, the least of all cases, and the peripheral zone contour overlap improved for only one histology slide near the prostate base. Patient 2 boundaries were unclear due to the large tumor

TABLE III. Average errors (with standard deviation in brackets) between feature points selected on *in vivo* and *ex vivo* 3D T2w images from two separate annotators, before and after DIR.

	Annotator 1			Annotator 2		
		Average error			Average error	
Patient	Number of feature points	Before DIR (mm)	After DIR (mm)	Number of feature points	Before DIR (mm)	After DIR (mm)
1	13	2.8 (1.5)	2.4 (1.5)	5	4.1 (0.7)	2.2 (0.7)
2	10	2.4 (0.9)	3.2 (2.2)	5	5.1 (1.6)	1.4 (0.4)
3	12	3.2 (1.4)	4.3 (1.8)	2	2.5 (1.0)	4.8 (0.7)
4	14	3.1 (1.3)	2.4 (1.5)	5	4.9 (2.1)	2.7 (1.9)
5	6	5.2 (1.6)	4.8 (1.2)	5	5.7 (2.2)	5.1 (2.7)
6	5	2.2 (0.9)	2.0 (1.6)	5	2.5 (0.5)	1.8 (0.5)
Average	**10**	**3.2 (1.3)**	**3.2 (1.6)**	**4.5**	**4.1 (1.4)**	**3.0 (1.1)**

crossing the peripheral zone boundary and entering the transition zone which made both pathology and MRI annotations challenging.

3.B. Histology to *ex vivo* MRI registration

Qualitative assessment of the registration between histology images and *ex vivo* MRI demonstrated a good alignment of images. Quantitative assessment showed that the distance between control points after registration gave a mean distance of 0.57 mm (SD 0.28 mm, range 0.06–1.99 mm). The mean scaling required to register histology with *ex vivo* MRI was 106.7% (SD 4.3%). Scale factors ranged from 97.6% to 121.5%, with one slide each at the apex from patient 1 and patient 5 reducing in size after registration. Figure 5(c) shows one example registered slice for patient 2, where the unannotated histology image and tumor mask are overlaid on the corresponding *ex vivo* MR image.

4. DISCUSSION

The aim of our study was to develop a registration framework to accurately map *in vivo* MRI with histology of the prostate using *ex vivo* MRI to provide an intermediate registration step. Whilst our sample size was small, our goal was to demonstrate that our registration methods were feasible across patients with prostates of differing sizes and shapes, and different tumor volumes (see Table I). Whilst registration can never be perfect, by using *ex vivo* MRI, we have ensured that a considerable number of prostate tissue deformation sources are accounted for. Furthermore, by acquiring *in vivo* and *ex vivo* 3D T2w images and convolving them with a LoG filter before applying deformable registration, we have developed a novel approach to align the prostate tissue before and after surgical removal. In contrast with a number of research groups who have simply mapped disease location by anatomical quadrant or investigated a section of the prostate such as the peripheral zone, our intent was to register MRI and histology of the entire prostate including tumor location and tumor biology, such as cell density, to give a voxel level representation of the entire gland.

Applying DIR to align the *in vivo* and *ex vivo* MR images was the most difficult task in the registration process, due to a number of inherent difficulties. First, the same tissue structures often had quite a different appearance in the *in vivo* and *ex vivo* 3D T2w MR images, despite the use of near identical scanning protocols. For example, the prostate boundary appeared bright in *ex vivo* 3D images in contrast to the dark boundary observed in the *in vivo* 3D images. This is in part due to the difference in water content between living and excised, formalin-fixed tissue. It is likely that use of the knee coil for the *ex vivo* imaging compared to the torso surface coil used for *in vivo* imaging also contributed to the difference in MR signal. Second, once the prostate is removed, it undergoes considerable distortion compared to the *in vivo* shape. Formalin fixation causes tissue shrinkage, which is not necessarily uniform throughout the different tissues in the prostate. Furthermore, the side of the prostate positioned at the bottom of the bucket of fixative after surgery may cause flattening on one side of the prostate.

By using the prostate contour masks and applying a LoG filter to the 3D T2w data, we ensured the DIR was guided by the prostate boundary and also driven by dominant features within the prostate as the smaller features did not correspond well. During method development, we assessed different filters including Sobel and Gabor filters, as well as different metrics including normalized cross correlation. Normalized mutual information was selected as the similarity metric due the fast computational time (less than 1 h to solve), and to account for differences in image brightness. We considered annotating additional features to further drive the registration including the peripheral zone boundary and the urethra; however, significant uncertainties in delineation rendered this process too subjective. Despite this, utilizing the LoG filter still ensured that prominent peripheral zone boundaries and urethra locations could be enhanced for registration. Results confirmed that the gross prostate volume matched more closely after DIR, demonstrated by the dice coefficient values for the prostate contour which increased for all study patients.

Selecting corresponding feature points to quantify the registration was a challenging task for both annotators, due to the limited resolution and partial volume effects in MRI which caused difficulties in defining the exact boundaries and centre points of spherical-type shapes and the different tissue

appearance in the *in vivo* and *ex vivo* 3D scans. It was not possible to quantify the exact error inherent in defining these points; however, based on our 3D T2w image resolution, estimating an error of one voxel in the selection of a point would result in an error of 0.6 mm. By applying this estimated error margin of 0.6 mm in feature point position, we observed that registration of the large and feature-rich prostate from patient 4 improved after DIR based on points from both annotators, while the registration of patient 3 who had a small and relatively homogeneous prostate got worse after DIR. Patient 2 had contradictory results from each annotator, where the feature point error difference was larger than the margin of 0.6 mm in both cases. Points from annotator 2 improved after DIR however annotator 1, who showed a worse feature point correspondence after DIR, found it particularly difficult to select feature points for this patient since there were a number of hyperintense features that were linear in shape rather than spherical so they could not always reliably identify the centre point.

The remaining three patients, patients 1, 5, and 6 all showed an improvement in feature point correspondence after DIR; however, the difference in feature point error from annotator 1 was all below the margin of 0.6 mm (range 0.2–0.5 mm) while the difference in error from annotator 1 all above the error margin (range 0.6–1.9 mm). In light of this, we compared the different methods used to select points by each annotator. Annotator 1 selected features in both the peripheral zone and transitional zone which frequently were located at the edge of visible nodules and prostate boundaries while annotator 2 mostly restricted point selection to the centre of hyperintense regions in the feature rich transitional zone. Based on the partial volume effects in MRI, the centre points of hyperintense regions were expected to be more reliable than features located at nodule edges. Hence, we concluded that our DIR methodology improved the registration in prostates with many visible features on 3D T2w imaging, whereas it did not appear as effective for prostates which were relatively homogeneous. In addition, it was difficult to validate registration accuracy in prostates with mostly linear rather than spherical shaped features.

Computing the overlap between peripheral zone regions provided an additional metric to assess the registration. While the average dice coefficient value increased from 0.69 to 0.75 after DIR, there was still a large portion of peripheral zone that did not overlap (i.e., 25%). The two main reasons for this were the following: (1) the peripheral zone is much easier to see on real tissue provided by histology in comparison with MRI, and (2) there were a number of interpolation and resampling steps required to transform the peripheral zone contour from *in vivo* axial T2w MRI to *ex vivo* axial MRI.

An estimate of the overall uncertainty between registered *in vivo* MRI and histology is possible by summing the mean errors in quadrature for each step in the registration process. The average distance between feature points from both annotators after DIR was 3.1 mm, which provides a 3D measure of error between *in vivo* and *ex vivo* MRI assuming there is no uncertainty associated with the selected feature points. The mean distance between control points on histology images and *ex vivo* MRI after automated registration was 0.57 mm, which provides an error estimate in the axial plane between these images. In order to estimate the uncertainty between *ex vivo* MRI and histology images in the out-of-plane direction, we have considered the pixel size on the T1 coronal images which were used to define the axial T2w MR image slice position. Since the T1 coronal images visualized the slots in the sectioning box across two pixels, equating to a thickness of 0.84 mm, we have conservatively rounded this value to predict an out-of-plane uncertainty of 1 mm. This also compensates for any error caused by microtome slicing during pathology processing which expected to be no more than 200 μm. Hence, when combining the 3D uncertainty vector lengths (*in vivo* to *ex vivo* and *ex vivo* to histology) in quadrature, we obtain a combined uncertainty estimate of 3.3 mm.

This estimated uncertainty is comparable to values reported by Park *et al.*[23] and marginally higher than errors of 2–3 mm reported by Groenendaal *et al.*[7] whose work was limited to the peripheral zone. Registration errors are typically incorporated into treatment margins for safe application of radiotherapy. Groenendaal *et al.*,[7] for example, recommended a 5 mm margin be implemented for tumors predicted in the peripheral zone from mpMRI. Our work suggests similar sized margins would be required; however, we plan to implement a personalized margin based on a user defined risk strategy. Furthermore, our conservative implementation of focal therapy will ensure that regions of the prostate determined to be at low risk of containing cancer will still receive a low dose of radiation to account for small tumors not detected through imaging.

We are currently working to improve the quality of our *in vivo* and *ex vivo* 3D T2w MRI data to improve the images for coregistration which may further reduce the uncertainties. This includes removal of the in-plane interpolation of the *ex vivo* 3D T2w images before image reconstruction, to reduce data smoothing. Furthermore, a systematic investigation of parameters utilized during DIR will carried out, and the benefit of applying the LoG filter versus no filter will be quantitatively assessed for a larger cohort of patients. A limitation of this study is the amount of manual annotation required, including pathologist markup, the initial manual alignment of *in vivo* and *ex vivo* images before DIR, and the prostate contour annotation which introduces subjectivity and more preprocessing of data before registration. We aim to automate these processes where possible, which would speed up processing and computation times for each patient, which is currently between 1 and 2 days. We are also working towards semiautomating tumor delineation on histology data using a combination of pathologist mark-up and computer assisted methods[34,35] which will be compared with tumor volumes in MRI defined by radiologists. Future work will include processing and image registration techniques to include features from histology such as cell density,[36] and mpMRI data including ADC maps from DWI, pharmacokinetic and parametric maps from DCE-MRI and R2* maps from BOLD MRI.

The *ex vivo* axial T2w MR image was selected as the reference dataset for each patient as this required no interpolation of the sparsely sampled histology data. In future, we will map all data to *in vivo* axial T2w MRI so we can develop an

in vivo anatomical and biological atlas of the prostate from a growing database of patients. Using this atlas, along with Bayesian inferential techniques and inverse biological optimization methods, we intend to develop focal therapy treatment plans which will target known tumors while giving a reduced radiation dose to surrounding prostate tissue.

5. CONCLUSION

We have successfully developed a registration process for mapping *in vivo* MRI of the prostate to histology data implementing a number of processing steps and *ex vivo* MRI of the prostate specimen to improve accuracy. All six patients in our sample dataset were registered, by taking into account each aspect of prostate deformation via a series of registration tasks to give histology images and *in vivo* MRI in the *ex vivo* MRI frame of reference. Results demonstrated that our novel DIR methodology between *in vivo* and *ex vivo* MRI using 3D T2w images convolved with a LoG filter improved accuracy in comparison with a manual alignment for prostates containing features which were readily visible on 3D T2w MRI; however, it was challenging to validate whether DIR improved registration for prostates with few or mostly linear rather than spherical shaped features. Refinement of our MR imaging protocols to improve the data resolution and signal to noise ratio in the *in vivo* and *ex vivo* 3D T2w MR images, is currently underway and is expected to improve results. While the sample size was small, this framework provides a robust method which we will apply to future study patients in order to build an atlas of the prostate anatomy and tumor biology. Correlated data from an increasing database of patients will be used to inform a radiobiological model of the prostate, to enable MRI based planning for prostate focal therapy treatment.

ACKNOWLEDGMENTS

Dr. Reynolds is funded by a Movember Young Investigator Grant awarded through Prostate Cancer Foundation of Australia's Research Program. Dr. Williams was partially supported by a Victorian Cancer Agency Fellowship. Work was supported by PdCCRS Grant No. 628592 with funding partners: Prostate Cancer Foundation of Australia and the Radiation Oncology Section of the Australian Government of Health and Aging and Cancer Australia. NICTA is funded by the Australian Government through the Department of Communications and the Australian Research Council through the ICT Centre of Excellence Program. Thanks to Dr. C. Meyers for assistance in initiating this project and Professor Martin Ebert for his contribution during project development and in paper preparation. The authors report no conflicts of interest. The authors alone are responsible for the content and writing of the paper.

[a]Author to whom correspondence should be addressed. Electronic mail: Hayley.Reynolds@petermac.org

[1]I. A. Donaldson, R. Alonzi, D. Barratt, E. Barret, V. Berge, S. Bott, D. Bottomley, S. Eggener, B. Ehdaie, M. Emberton, R. Hindley, T. Leslie, A. Miners, N. McCartan, C. M. Moore, P. Pinto, T. J. Polascik, L. Simmons, J. van der Meulen, A. Villers, S. Willis, and H. U. Ahmed, "Focal therapy: Patients, interventions, and outcomes—A report from a consensus meeting," Eur. Urol. **67**(4), 771–777 (2015).

[2]S. Langley, H. U. Ahmed, B. Al-qaisieh, D. Bostwick, L. Dickinson, F. G. Veiga, P. Grimm, S. Machtens, F. Guedea, and M. Emberton, "Report of a consensus meeting on focal low dose rate brachytherapy for prostate cancer," BJU Int. **109**(Suppl. 1), 7–16 (2012).

[3]J. M. Cosset, X. Cathelineau, G. Wakil, N. Pierrat, O. Quenzer, D. Prapotnich, E. Barret, F. Rozet, M. Galiano, and G. Vallancien, "Focal brachytherapy for selected low-risk prostate cancers: A pilot study," Brachytherapy **12**(4), 331–337 (2013).

[4]A. Borren, G. Groenendaal, M. R. Moman, A. E. Boeken Kruger, P. J. van Diest, M. van Vulpen, M. E. P. Philippens, and U. A. van der Heide, "Accurate prostate tumor detection with multiparametric magnetic resonance imaging: Dependence on histological properties," Acta Oncol. **53**(1), 88–95 (2014).

[5]A. Haworth, S. Williams, H. Reynolds, D. Waterhouse, G. M. Duchesne, J. Bucci, D. Joseph, S. Bydder, and M. Ebert, "Validation of a radiobiological model for low-dose-rate prostate boost focal therapy treatment planning," Brachytherapy **12**(6), 628–636 (2013).

[6]D. L. Langer, T. H. van der Kwast, A. J. Evans, A. Plotkin, J. Trachtenberg, B. C. Wilson, and M. A. Haider, "Prostate tissue composition and MR measurements: Investigating the relationships between ADC, T2, K(trans), v(e), and corresponding histologic features," Radiology **255**(2), 485–494 (2010).

[7]G. Groenendaal, M. R. Moman, J. G. Korporaal, P. J. Van Diest, M. Van Vulpen, M. E. P. Philippens, and U. A. van der Heide, "Validation of functional imaging with pathology for tumor delineation in the prostate," Radiother. Oncol. **94**(2), 145–150 (2010).

[8]G. Groenendaal, A. Borren, M. R. Moman, E. Monninkhof, P. J. van Diest, M. E. P. Philippens, M. van Vulpen, and U. A. van der Heide, "Pathologic validation of a model based on diffusion-weighted imaging and dynamic contrast-enhanced magnetic resonance imaging for tumor delineation in the prostate peripheral zone," Int. J. Radiat. Oncol., Biol., Phys. **82**(3), e537–e544 (2012).

[9]B. Turkbey, P. A. Pinto, H. Mani, M. Bernado, Y. Pang, Y. L. McKinney, K. Khurana, G. C. Ravizzini, P. S. Albert, M. J. Merino, and P. L. Choyke, "Prostate cancer: Value of multiparametric MR imaging at 3T for detection—Histopathologic correlation," Radiology **255**(1), 89–99 (2010).

[10]B. Zelhof, M. Pickles, G. Liney, P. Gibbs, G. Rodrigues, S. Kraus, and L. Turnbull, "Correlation of diffusion-weighted magnetic resonance data with cellularity in prostate cancer," BJU Int. **103**(7), 883–888 (2008).

[11]P. J. Hoskin, D. M. Carnell, N. J. Taylor, R. E. Smith, J. J. Stirling, F. M. Daley, M. I. Saunders, S. M. Bentzen, D. J. Collins, J. A. d'Arcy, and A. P. Padhani, "Hypoxia in prostate cancer: Correlation of BOLD-MRI with pimonidazole immunohistochemistry-initial observations," Int. J. Radiat. Oncol., Biol., Phys. **68**(4), 1065–1071 (2007).

[12]R. Alonzi, A. Padhani, J. Taylor, J. Stirling, B. Wilton, J. d'Arcy, D. Collins, M. Saunders, and P. Hoskin, "Sensitivity and specificity of functional MRI to map tumor hypoxia in the human prostate gland," in *Proceedings of the International Society for Magnetic Resonance in Medicine* (Mira Digital Publishing, Saint Louis, MO, 2008), p. 167. Available at http://cds.ismrm.org/ismrm-2008/isv7/main.htm.

[13]P. Gibbs, G. P. Liney, M. D. Pickles, B. Zelhof, G. Rodrigues, and L. W. Turnbull, "Correlation of ADC and T2 measurements with cell density in prostate cancer at 3.0 Tesla," Invest. Radiol. **44**(9), 572–576 (2009).

[14]C. Meyer, B. Ma, L. P. Kunju, M. Davenport, and M. Piert, "Challenges in accurate registration of 3-D medical imaging and histopathology in primary prostate cancer," Eur. J. Nucl. Med. Mol. Imaging **40**(Suppl. 1), S72–S78 (2013).

[15]J. Chappelow, B. N. Bloch, N. Rofsky, E. Genega, R. Lenkinski, W. DeWolf, and A. Madabhushi, "Elastic registration of multimodal prostate MRI and histology via multiattribute combined mutual information," Med. Phys. **38**(4), 2005–2018 (2011).

[16]G. Nir, R. S. Sahebjavaher, P. Kozlowski, S. D. Chang, E. C. Jones, S. L. Goldenberg, and S. E. Salcudean, "Registration of whole-mount histology and tomography of the prostate using particle filtering," IEEE Trans. Med. Imaging **33**(8), 1601–1613 (2014).

[17]B. Turkbey, H. Mani, V. Shah, A. R. Rastinehad, M. Bernardo, T. Pohida, Y. Pang, D. Daar, C. Benjamin, Y. L. McKinney, H. Trivedi, C. Chua, G. Bratslavsky, J. H. Shih, W. M. Linehan, M. J. Merino, P. L. Choyke, and

P. A. Pinto, "Multiparametric 3T prostate magnetic resonance imaging to detect cancer: Histopathological correlation using prostatectomy specimens processed in customized magnetic resonance imaging based molds," J. Urol. **186**(5), 1818–1824 (2011).
[18]C. Hughes, O. Rouvière, F. Mege-Lechevallier, R. Souchon, and R. Prost, "Robust alignment of prostate histology slices with quantified accuracy," IEEE Trans. Biomed. Eng. **60**(2), 281–291 (2013).
[19]S. Y. Kimm, T. V. Tarin, J. H. Lee, B. Hu, K. Jensen, D. Nishimura, and J. D. Brooks, "Methods for registration of magnetic resonance images of *ex vivo* prostate specimens with histology," J. Magn. Reson. Imaging **36**(1), 206–212 (2012).
[20]A. D. Ward, C. Crukley, C. A. McKenzie, J. Montreuil, E. Gibson, C. Romagnoli, J. A. Gomez, M. Moussa, J. Chin, G. Bauman, and A. Fenster, "Prostate: Registration of digital histopathologic images to *in vivo* MR images acquired by using endorectal receive coil," Radiology **263**(3), 856–864 (2012).
[21]G. Nir, R. S. Sahebjavaher, P. Kozlowski, S. D. Chang, and R. Sinkus, "Model-based registration of *ex vivo* and *in vivo* MRI of the prostate using elastography," IEEE Trans. Med. Imaging **32**(7), 1349–1361 (2013).
[22]N. Samavati, D. McGrath, J. Lee, T. van der Kwast, M. Jewett, C. Ménard, and K. K. Brock, "Biomechanical model-based deformable registration of MRI and histopathology for clinical prostatectomy," J. Pathol. Inform. **2**, S10 (11pp.) (2011).
[23]H. Park, M. R. Piert, A. Khan, R. Shah, H. Hussain, J. Siddiqui, T. L. Chenevert, and C. R. Meyer, "Registration methodology for histological sections and *in vivo* imaging of human prostate," Acad. Radiol. **15**(8), 1027–1039 (2008).
[24]H. Park, C. R. Meyer, D. Wood, A. Khan, R. Shah, H. Hussain, J. Siddiqui, J. Seo, T. Chenevert, and M. Piert, "Validation of automatic target volume definition as demonstrated for 11 C-Choline PET/CT of human prostate cancer using multi-modality fusion techniques," Acad. Radiol. **17**(5), 614–623 (2011).
[25]J. O. Barentsz, J. Richenberg, R. Clements, P. Choyke, S. Verma, G. Villeirs, O. Rouviere, V. Logager, and J. J. Fütterer, "ESUR prostate MR guidelines 2012," Eur. Radiol. **22**(4), 746–757 (2012).
[26]H. Johnson, G. Harris, and K. Williams, "BRAINSFit: Mutual information rigid registrations of whole-brain 3D images, using the insight toolkit," Insight J. 1–10 (2007), available at http://hdl.handle.net/1926/1291.
[27]A. Fedorov, R. Beichel, J. Kalpathy-Cramer, J. Finet, J. C. Fillion-Robin, S. Pujol, C. Bauer, D. Jennings, F. Fennessy, M. Sonka, J. Buatti, S. Aylward, J. V. Miller, S. Pieper, and R. Kikinis, "3D SLICER as an image computing platform for the quantitative imaging network," Magn. Reson. Imaging **30**(9), 1323–1341 (2012).
[28]D. Sage, F. R. Neumann, F. Hediger, S. M. Gasser, and M. Unser, "Automatic tracking of individual fluorescence particles: Application to the study of chromosome dynamics," IEEE Trans. Image Process. **14**(9), 1372–1383 (2005).
[29]C. A. Schneider, W. Rasband, and K. W. Eliceiri, "NIH image to ImageJ: 25 years of image analysis," Nat. Methods **9**, 671–675 (2012).
[30]C. Orczyk, S. S. Taneja, H. Rusinek, and A. B. Rosenkrantz, "Assessment of change in prostate volume and shape following surgical resection through co-registration of *in-vivo* MRI and fresh specimen *ex-vivo* MRI," Clin. Radiol. **69**(10), e398–e403 (2014).
[31]D. Rueckert, L. I. Sonoda, C. Hayes, D. L. Hill, M. O. Leach, and D. J. Hawkes, "Nonrigid registration using free-form deformations: Application to breast MR images," IEEE Trans. Med. Imaging **18**(8), 712–721 (1999).
[32]T. Rohlfing and C. R. Maurer, "Nonrigid image registration in shared-memory multiprocessor environments with application to brains, breasts, and bees," IEEE Trans. Inf. Technol. Biomed. **7**(1), 16–25 (2003).
[33]E. Gibson, C. Crukley, M. Moussa, J. L. Chin, G. Bauman, A. Fenster, and A. D. Ward, "Validation of direct registration of whole-mount prostate digital histopathology to *ex vivo* MR images," in *Prostate Cancer Imaging*, Lecture Notes in Computer Science Vol. 6963, edited by A. Madabhushi, J. Dowling, H. Huisman, and D. Barratt (Springer-Verlag, Berlin Heidelberg, 2011), pp. 134–145.
[34]M. D. Difranco, G. O'Hurley, E. W. Kay, R. W. G. Watson, and P. Cunningham, "Ensemble based system for whole-slide prostate cancer probability mapping using color texture features," Comput. Med. Imaging Graphics **35**, 629–645 (2011).
[35]M. D. DiFranco, H. M. Reynolds, C. Mitchell, S. Williams, P. Allan, and A. Haworth, "Performance assessment of automated tissue characterization for prostate H & E stained histopathology," Proc. SPIE **9420**, 94200M (2015).
[36]H. M. Reynolds, S. Williams, A. M. Zhang, C. S. Ong, D. Rawlinson, R. Chakravorty, C. Mitchell, and A. Haworth, "Cell density in prostate histopathology images as a measure of tumor distribution," Proc. SPIE **9041**, 90410S (2014).